NIH Public Access
Author Manuscript
*Contrast Media Mol Imaging*. Author manuscript; available in PMC 2015 September 01.

Published in final edited form as:
*Contrast Media Mol Imaging*. 2014 September ; 9(5): 333–341. doi:10.1002/cmmi.1579.

# Sub-second Proton Imaging of $^{13}$C Hyperpolarized Contrast Agents in Water

**Milton L. Truong**[a], **Aaron M. Coffey**[a,b], **Roman V. Shchepin**[a], **Kevin W. Waddell**[a,c], and **Eduard Y. Chekmenev**[*,a,b,d,e]

[a]Department of Radiology, Vanderbilt University Institute of Imaging Science (VUIIS), Nashville, Tennessee, 37232, United States

[b]Department of Biomedical Engineering, Vanderbilt University, Nashville, Tennessee, 37235, United States

[c]Department of Physics, Vanderbilt University, Nashville, Tennessee, 37235, United States

[d]Department of Biochemistry, Vanderbilt University, Nashville, Tennessee, 37205, United States

[e]Vanderbilt-Ingram Cancer Center, Vanderbilt University, Nashville, Tennessee, 37232, United States

## Abstract

Indirect proton detection of $^{13}$C hyperpolarized contrast agents potentially enables greater sensitivity. Presented here is a study of sub-second projection imaging of hyperpolarized $^{13}$C contrast agent addressing the obstacle posed by water suppression for indirect detection in vivo. Sodium acetate phantoms were used to develop and test water suppression and sub-second imaging with frequency selective RF pulses using spectroscopic and imaging indirect proton detection. A 9.8 mM aqueous solution of $^{13}$C PHIP hyperpolarized 2-hydroxyethyl-$^{13}$C-propionate-$d_{2,3,3}$ (HEP), $<P>\sim$25% was used for demonstration of indirect proton sub-second imaging detection. Balanced 2D FSSFP (Fast Steady State Free Precession) allowed recording proton images with FOV = 64×64 mm$^2$ and spatial resolution 2×2 mm$^2$ with total acquisition time of less than 0.2 s. In thermally polarized sodium 1-$^{13}$C-acetate, $^{13}$C to $^1$H polarization transfer efficiency of 45.1% of the theoretically predicted values was observed in imaging detection corresponding to an 11 fold of overall sensitivity improvement compared to direct $^{13}$C FSSFP imaging. $^{13}$C to $^1$H polarization transfer efficiency of 27% was observed in imaging detection corresponding to a 3.25 fold sensitivity improvement compared to direct $^{13}$C FSSFP imaging with hyperpolarized HEP. The range of potential applications and limitations of this sub-second and ultra-sensitive imaging approach are discussed.

### Keywords

NMR; Hyperpolarization; Contrast Agent; sub-second imaging; 13C; indirect detection; parahydrogen; PHIP

[*]Corresponding Author: *For E.Y.C.: phone, +1-615-322-1329; fax, +1-626-322-0734; eduard.chekmenev@vanderbilt.edu.

NIH-PA Author Manuscript
NIH-PA Author Manuscript
NIH-PA Author Manuscript

NIH-PA Author Manuscript
NIH-PA Author Manuscript
NIH-PA Author Manuscript



## 1. Introduction

Hyperpolarization techniques increase MR sensitivity by several orders of magnitude (1). In principle, many nuclear spins can be hyperpolarized including $^{19}F$, $^{1}H$, $^{15}N$, and $^{13}C$. Abundant protons in biologically relevant molecules such as lactate have the largest magnetic moments and MR Larmor frequencies and therefore, should be superior from a detection perspective. However, biomedical use of hyperpolarized in vivo contrast agents require a significant time scale on the order of tens of seconds for contrast agent manipulation and in vivo delivery from the site of injection to the volume of interest (e.g. tumor) (2). The delay between synthesis of the hyperpolarized state and delivery in vivo is long compared to the typical lifetime of protons (~ 2 sec), therefore precluding direct detection of hyperpolarized protons. For example, if $T_1$ is 2 s, polarization decreases by ~400 fold after 12 s. As a result, long-lived nuclear spin sites, e.g. carboxyl $^{13}C$, are prepared by dissolution Dynamic Nuclear Polarization (DNP) (3) directly. In contrast, in parahydrogen induced polarization (PHIP) (4), the initial singlet state of nascent parahydrogen protons is converted to magnetization on a longer lived nuclear spin (e.g. carboxyl $^{13}C$) (5). Regardless of preparation, this heteronuclear storage nucleus is subsequently detected directly by $^{13}C$ NMR to interrogate metabolism in vivo (6). Examples include 1-$^{13}C$-pyruvate (7), 1-$^{13}C$-succinate (8), 1-$^{13}C$-glutamine (9) and others.

Despite nearly perfect polarization $P \rightarrow 100\%$ achieved by dissolution DNP and PASADENA (Para-Hydrogen and Synthesis Allow Dramatically Enhanced Nuclear Alignment) (10), sensitivity could be further improved by reading out heteronuclear magnetization on protons. Protons are inherently more sensitive under conditions of identical polarization and $T_2$*, because of the other two gamma factors: greater resonant frequency and larger magnetic moment. This results in a combined enhancement of up to 15.7 fold, $(\gamma_{1H}/\gamma_{13C})^2$, not accounting for $T_2$*, RF coil sensitivity, and subject noise.

Other, more practical factors, make $^{13}C$ detection challenging. $(\gamma_{1H}/\gamma_{13C})^2$ more gradient power is required to achieve the same spatial resolution as in conventional MRI. In addition, all clinical and preclinical MRI scanners are equipped with $^{1}H$ detection as a standard feature, while $^{13}C$ requires specialized hardware and software. The latter can actually become a major impediment to the widespread use of hyperpolarized contrast agents.

Proton detection of $^{13}C$ hyperpolarized contrast agents can solve the above challenges by the use of pulse sequences requiring only RF $^{13}C$ excitation. The latter requires significantly less demanding hardware and can potentially provide more than an order of magnitude sensitivity gain. This additional sensitivity gain would be helpful even in hyperpolarized MR, because it can improve spatial resolution, decrease the dose of contrast agents, and therefore potentially allow for deeper penetration of metabolic fluxes.

Candidate polarization transfer sequences for reading out hyperpolarized heteronuclear magnetization can be found from high-resolution NMR, such as DEPT (Distortionless Enhancement by Polarization Transfer), INEPT (Insensitive Nuclei Enhanced by Polarization Transfer), and others. Here, conventional INEPT was chosen (11), and specifically a refocused INEPT sequence, which can theoretically provide detection

NIH-PA Author Manuscript

NIH-PA Author Manuscript

NIH-PA Author Manuscript

sensitivity enhancements of up to $(\gamma_{1H}/\gamma_{13C})^2$, where $\gamma_{1H}$ and $\gamma_{13C}$ are gyromagnetic ratios of detection and polarization storage nuclear spin sites. The INEPT sequence was chosen due to its relative simplicity and known utility in clinical research (12).

The concept of a more sensitive, indirect proton detection was demonstrated for highly polarized $^{13}$C PHIP contrast agents (13) as well as DNP polarized contrast agents spectroscopically (14) and more recently using fast imaging sequences (15). However, the vast majority of these experiments were performed in $D_2O$ to suppress background signals from water and other protons. DNP coupled with polarization transfer techniques have been shown to effectively transfer polarization in a multidimensional framework (16–18) including a recent study with DNP hyperpolarized $^{13}$C-acetate *in vivo* (17). However, the demonstrated polarization transfer efficiency was rather low (17). It should be noted, however, that the choice of 1-$^{13}$C-acetate in our in vitro studies was determined by the recent use of its hyperpolarized form for studying metabolism *in vivo* (19–21).

Translation of this approach *in vivo* requires sequence development for proton imaging of dilute millimolar proton spins in the presence of > 50 M water. The work presented here demonstrates sub-second proton imaging of $^{13}$C hyperpolarized contrast agent in water medium. A 25% polarized contrast agent at ~10 mM concentration was used to simulate in vivo conditions of highly polarized contrast agent with low concentration and decaying non-equilibrium hyperpolarization.

High polarization transfer efficiency and 2×2 mm$^2$ in-plane resolution were achieved. The prospects of pre-clinical translation, method potential and limitations for high and low magnetic fields are discussed from the perspective of metabolic imaging of cancer. Other polarization transfer approaches (22,23) can be used to further maximize the use of nonrenewable hyperpolarization.

## 2. Materials and Methods

### 2.1. Phantom Preparation for Boltzmann polarization studies

Sodium acetate and sodium 1-$^{13}$C-acetate (99% atom $^{13}$C) were obtained from Isotec-Sigma-Aldrich Corporation (Miamisburg, OH), and concentrated to 4.3 M in $H_2O$ and 99.8% $D_2O$ respectively. Spherical phantom plastic containers were fully filled for each sample to a total solution volume of 2.8 mL.

### 2.2. Phantom preparation for hyperpolarized studies

2-hydroxyethyl-1-$^{13}$C-acrylate-$d_{2,3,3}$ (HEA) was hydrogenated using a home-built PHIP polarizer with *in situ* detection capability operating at 5.9 mT. This device (Coffey, A. M. et al., unpublished results) is similar to our previously published polarizer operating at 47.5 mT using PASADENA (parahydrogen and synthesis allow dramatically enhanced nuclear alignment) (24,25). Production of PHIP hyperpolarized 2-hydroxyethyl-$^{13}$C-propionate-$d_{2,3,3}$ (HEP) has been previously described by us (5,24–26) and others (27). Briefly, parahydrogen gas was produced with a custom lab-built generator by pulsing ambient ortho-hydrogen into an iron oxide catalyst filled chamber at 14–20 K (26). This enriched parahydrogen gas was then added to unsaturated molecular precursors using water-soluble

NIH-PA Author Manuscript

NIH-PA Author Manuscript

NIH-PA Author Manuscript

rhodium(I) based molecular catalysts (28,29) in a high pressure chemical reactor. 1,4-bis[(phenyl-3-propanesulfonate)phosphine]butane, disodium salt (717347, Sigma-Aldrich-Isotec, OH, USA) and bis (norbornadiene) rhodium (I) tetrafluoroborate (45–0230, Strem Chemicals, MA, USA) were used for hydrogenation catalyst preparation in water medium as described earlier (5). PHIP precursor, HEA, was added to the aqueous solution after catalyst preparation. The concentration for the hyperpolarized product, HEP, was 9.8 mM, with an average hyperpolarization level of 25% at the $^{13}$C site measured *in situ*. Approximately 4 mL of aqueous solution containing hyperpolarized HEP was produced and transferred to a plastic syringe in the fringe field of a 4.7 T MR scanner, where $^{13}$C $T_1$ = 50 s (30). The hyperpolarized material was injected into a 2.8 mL hollow polypropylene sphere near the bore of the scanner and placed inside the RF coil, with a total delivery time of ~50 s.

### 2.3. Spectroscopy and Imaging

All spectroscopy and imaging experiments were performed on a Varian 4.7 T animal imaging system using the VNMRJ version 3.2 software suite. The experiments were conducted with a custom-built 38 mm ID two-channel RF coil, dual-tuned to $^{1}$H (200.25 MHz) and $^{13}$C (50.25 MHz). All the experiments used the shim gradient values obtained from shimming a 2.8 mL sample of deionized water in a plastic spherical phantom container, resulting in a half-height line width of 4 Hz. Once the magnetic field was shimmed, the shim sample was swapped with the experimental samples, with care taken to replicate the sample position in the RF coil and the RF coil position in the magnet as used for shimming so that the magnetic field optimizations were accurately reflected across all the samples. Phantom replacement was necessary for hyperpolarized experiments, because the lifetime of hyperpolarization prevented shimming on individual samples.

All $^{1}$H and $^{13}$C spectroscopic experiments consisted of a single acquisition with 1 s of acquisition time, 10 kHz spectral width, 10,000 complex points, and calibrated 90° excitation RF pulse. The INEPT delay for sodium acetate was $\tau_{INEPT}$ = 42 ms and the refocusing delay was $\tau_{refocus}$ = 16 ms for $^{1}$H to $^{13}$C polarization transfer in the $^{13}$C-$CH_3$ molecular framework with $J^2_{CH}$ = 6.0 Hz (11). The INEPT delay for sodium acetate was $\tau_{INEPT}$ = 17 ms and the refocusing delay was $\tau_{refocus}$ = 35 ms for one $^{13}$C to three protons polarization transfer in the $^{13}$C-$CH_3$ molecular framework with $J^2_{CH}$ = 6.0 Hz. For hyperpolarized HEP, the polarization transfer from $^{13}$C to two protons derived from parahydrogen in the $^{13}$C-CH-CH molecular framework used delays of $\tau_{INEPT}$ = 20 ms and $\tau_{refocus}$ = 16 ms as determined previously (13) based on prior knowledge of the spin-spin couplings (27). In all imaging and spectroscopic experiments, the generic refocused INEPT sequence was augmented by $\tau_{-90y}$ at the end of the second refocus delay as shown in Fig. 1a on the detection channel to prepare magnetization along the *z*-axis for subsequent detection with frequency selective RF pulses using spectroscopic or imaging acquisition.

All imaging sequences used Varian's version of 2D FSSFP with single slice acquisition. Slice thickness was set to 60 mm to encompass the entire phantom. 90° acquisition flip angle and 50 kHz spectral width were used for $^{13}$C and $^{1}$H imaging. Other imaging parameters such as TR/TE varied depending on the frequency selective excitation pulses. All $^{13}$C FSSFP images were acquired with 96×96 mm$^2$ FOV with 3×3 mm$^2$ spatial

NIH-PA Author Manuscript

NIH-PA Author Manuscript

NIH-PA Author Manuscript

resolution with $\tau_{90°}$ = 52.5 μs at 51.9 W and TR = 2.00 ms, TE = 1.00 ms with total acquisition time of 64 ms. $^{1}$H $\tau_{90°}$ was 57 μs and $^{1}$H $\tau_{180°}$ was 114 μs at 51.9 W for all non-frequency selective RF pulses. $^{1}$H frequency selective RF pulses were $^{1}$H $\tau_{90°}$ = 4.35 ms at 50.7 mW. Refocused INEPT polarization transfer blocks did not use frequency selective RF pulses. When $^{1}$H frequency selective RF pulses were used during imaging, TR/TE increased from 1.91/0.95 ms (no frequency selection) to 6.20/3.10 ms (with frequency selection) respectively. All $^{1}$H FSSFP images were acquired with 64×64 mm$^2$ FOV with 2×2 mm$^2$ spatial resolution with total imaging time of 61.1 ms (no frequency selection) and 198 ms (with frequency selection). Refocused INEPT polarization transfer imaging experiments utilized the same delays as described in the spectroscopy experiments.

## 3. Results

### 3.1. Heteronuclear Polarization From Three Methyl Protons to $^{13}$C in Isolated Methyl Group, Sodium 1-$^{13}$C-Acetate Phantom in $D_2O$: Imaging and Spectroscopy

The experimental polarization enhancement $\varepsilon_{exp}$ can be calculated as the ratio of $S_{INEPT}$ (see Supporting Information for details) and $S_{thermal}$, the signal intensities of the corresponding refocused INEPT and thermal experiments:

$$\varepsilon_{exp} = \frac{s_{INEPT}}{s_{thermal}} \quad (2)$$

Spectroscopic detection resulted in $\varepsilon_{exp}$ = 3.23 for INEPT transfer from $^{1}$H→$^{13}$C. This translates to 70% polarization transfer efficiency, $\eta = \varepsilon_{exp}/\varepsilon_{theory}$, for the refocused INEPT sequence when compared to the theoretical enhancement value, 4.59 (Supporting Information).

When refocused INEPT was coupled with the FSSFP fast imaging sequence at 4.7 T, Fig. 2, the magnitude of the INEPT enhanced image was increased with $\varepsilon_{exp}$ = 3.99, corresponding to $\eta$ = 87%, Figs. 1d and 1e. Imaging values of $\varepsilon_{exp}$ and $\eta$ were different from those of spectroscopic acquisition due to the relatively low SNR of $^{13}$C images acquired with thermal levels of $^{13}$C polarization.

### 3.2. $^{1}$H Background Suppression Using Multiband RF Excitation Pulses and $^{1}$H Pre-saturation: Imaging and Spectroscopy

The approach of using water presaturation along with frequency selective Gaussian RF pulses was adopted to test water suppression in the phantom sample containing 2.8 mL of water, Fig. S1 (see Supporting Information for details). A 2 s presaturation pulse block (square RF pulse block at 1.6 W) coupled with a 50 mW Gaussian detection pulse was applied with an offset frequency of 750 Hz upfield from the water frequency. Spectroscopically, this approach resulted in 99.88% reduction of the background water signal for the water phantom when compared with a baseline single pulse MR spectrum (Figs. S1a and S1b), as determined through signal integration. Additionally, when the water suppression scheme was coupled to FSSFP, the resulting MR images produced the same

NIH-PA Author Manuscript

NIH-PA Author Manuscript

NIH-PA Author Manuscript

result (Figs. S1c and S1d). The intensity of the water image was diminished from 101.5 a.u. without water suppression to 1.36 a.u. with suppression.

### 3.3. Proton Indirect Detection in Sodium Acetate Phantoms: Imaging and Spectroscopy

To examine the ability to indirectly detect protons from stored $^{13}C$ magnetization, a series of experiments were conducted using refocused INEPT coupled with the frequency selective water suppression method discussed above. A single scan MR spectrum and MR image of a 1-$^{13}C$-acetate phantom in water provided a baseline for examining $^{13}C$ polarization transfer efficiency and water suppression. With a peak integral value of nearly $1.19 \bullet 10^8$ a.u., the water peak from the baseline spectrum (Fig. 3a) overshadowed the acetate signal, $1.26 \bullet 10^7$ a.u., and resulted in an image where the voxel intensities were dominated by water proton magnetization. Next, $^1H$ signal from acetate methyl protons was detected after polarization transfer from pre-polarized $^{13}C_1$ (see above). The sequence (Fig. 2) started with multiband proton presaturation followed by the refocused INEPT sequence block ($^{13}C_1 \rightarrow {}^1H$), and ended with either spectroscopic or imaging $^1H$ detection using a frequency selective Gaussian shaped RF pulse as described above. The multiband proton suppression block was different from the one used in Fig. 2 in its use of a series of 50 ms-long RF pulses of identical amplitude but frequency alternating between the resonant frequencies of water and the methyl peaks of 1-$^{13}C$-acetate. The resulting spectrum (Fig. 3c) showed nearly full suppression, 99.83%, of the water peak, while maintaining 40% of the baseline acetate signal integral value. This trend was also confirmed in a follow-up study of a 1-$^{13}C$-acetate phantom in $D_2O$ (Fig. 3e). Indirect detection of $^{13}C$ magnetization using proton MRI images with multiband $^1H$ presaturation and Gaussian RF excitation pulse is shown in Figs. 3d and 3f with SNR of 144.7 and 197.2 for 1-$^{13}C$-acetate in $H_2O$ and 1-$^{13}C$-acetate in $D_2O$ respectively. Additionally identical spectroscopy and imaging studies were conducted on a sample of sodium acetate with natural abundance enrichment level of $^{13}C$ and the same concentration and volume as used in both the experiments involving $^{13}C$ sodium acetate in water and in $D_2O$. By testing a natural abundance sample with the INEPT enhanced pulse sequence, the resulting spectrum and image (Figs. 3g and 3h) with little to no signal assured that the sequence is performing properly and that the resulting images (Figs. 3d and 3f) were not from background water protons. The natural abundance sample contains vanishing quantity of $^{13}C$ spin labels, ~1/91$^{th}$ of that in Figs. 3c–f, which is likely responsible for a small signal seen in Fig. 3g.

From a theoretical perspective, for 1-$^{13}C$-acetate polarization transfer from $^{13}C \rightarrow {}^1H$ can be expressed with the equation:

$$P_{1H}^{INEPT} = \sin(2J_{HC}\tau_{INEPT}) \bullet \cos^2(2\pi J_{HC}\tau_{INEPT}) \bullet \sin(2\pi J_{HC}\tau_{refocus}) \bullet P_{13C} \quad (3)$$

For $^{13}C$-sodium acetate, the $J$-coupling between $^{13}C_1$ and $^1H$ is 6 Hz, and when $\tau_{INEPT}$ =17 ms and $\tau_{refocus}$ =35 ms, $P_{1H}$ reaches the maximum value of $0.372 \bullet P_{13C}$. The value of $P_{13C}$ was boosted by a refocused INEPT $^1H \rightarrow {}^{13}C$ pre-polarization of $^{13}C$ as described above. This improves $P_{13C}$, which without pre-polarization would be 0.251 that of $P_{1H}$ at equilibrium.

NIH-PA Author Manuscript

NIH-PA Author Manuscript

NIH-PA Author Manuscript

The experimental polarization transfer enhancement for indirect $^{1}$H detection can be calculated similarly to Eq. 2 with modification accounting for artificially boosted $^{13}$C polarization above the thermal level used in our experiments:

$$\varepsilon_{exp}=\frac{P^{1H}_{INEPT}}{P^{13C}}, \quad (4)$$

where $P_{13C}$ is nuclear spin polarization of $^{13}$C immediately before the refocused INEPT transfer procedure and $P^{1H}_{INEPT}$ is experimentally detected $^{1}$H polarization calculated as follows:

$$P^{1H}_{INEPT}=\frac{s^{1H}_{INEPT}}{s^{1H}_{thermal}} \bullet P^{1H}_{thermal}, \quad (5)$$

where $S^{1H}_{INEPT}$ is imaging or spectroscopic signal detected after INEPT transfer, $P^{1H}_{thermal}$ is the equilibrium thermal polarization of $^{1}$H spins, and $S^{1H}_{thermal}$ is corresponding imaging or spectroscopic signal detected using identical acquisition protocol as $S^{1H}_{INEPT}$. For the refocused INEPT transfer from $^{13}\mathrm{C} \rightarrow {}^{1}\mathrm{H}$ between the $^{13}\mathrm{C}_1$ and three methyl protons of acetate, $\varepsilon_{exp}$ is 0.367 for spectroscopic acquisition, 0.320 for imaging detection in $D_2O$ and 0.167 for imaging detection in $H_2O$ corresponding to polarization efficiency $\eta$ values of 98.6%, 85.9% and 45.1% respectively.

### 3.4. $^{13}$C and Indirect $^{1}$H Detection of Aqueous $^{13}$C Hyperpolarized Contrast Agent: Imaging and Spectroscopy

Single scan FSSFP $^{13}$C imaging was performed to determine the hyperpolarization levels for $^{13}$C HEP (Fig. 4a). The $^{13}$C hyperpolarization level was calculated to be *%P* = 5.3% at 4.7 T (Fig. 4a) after ~50–60 seconds of delivery time from the polarizer to the MRI scanner using Eq. 6, which compares FSSFP images of hyperpolarized $^{13}$C contrast agent (Fig. 4a) and reference compound (Fig. 1e) with known values of polarization using the same imaging parameters according to:

$$\%P_x=\varepsilon \cdot P^0_X \cdot 100\%=\frac{s_X \cdot \chi_{REF}}{s_{REF} \cdot \chi_X} P_{REF} \cdot 100\%, \quad (6)$$

where $P^0_X$ is the nuclear polarization at equilibrium at 298 K and 4.7 T, and the enhancement $\varepsilon$ is determined using the second part of this equation with measured signal, $S_{REF}$ (reference) and $S_X$ (hyperpolarized), and quantity information from reference compound $\chi_{REF}$ and the hyperpolarized agent $\chi_X$ of the same X nucleus, where X = $^{1}$H or $^{13}$C. With $B_0$ = 4.7 T and T = 298 K, $P^0_{13C}$ is 4.055*10$^{-6}$ and $P^0_{1H}$ is 1.61*10$^{-5}$. The 5.3% $^{13}$C hyperpolarization of HEP detected at 4.7 T correlates to an enhancement of 13,200 fold when compared to equilibrium $P^0_{13C}$ of 1-$^{13}$C-acetate at 4.7 T. The hyperpolarized $^{13}$C image of HEP had maximum SNR of 177. To demonstrate the relatively short lifetime of $^{13}$C HEP hyperpolarization, a $^{13}$C single slice FSSFP experiment (Fig. 4b) was followed by an identical imaging acquisition 90 s

NIH-PA Author Manuscript

NIH-PA Author Manuscript

NIH-PA Author Manuscript

after the first scan, resulting in no detectable signal in the image, signifying a full decay of $^{13}C$ hyperpolarization in HEP. 90 s delay corresponds to approximately $2x T_1$.

For indirect $^{1}H$ imaging of $^{13}C$ hyperpolarized HEP upon delivery to the 4.7 T scanner magnet, polarization was transferred from $^{13}C$ to the nascent protons via refocused INEPT using the same imaging sequence with proton multiband presaturation and selective RF excitation pulses as was used in the acetate studies above. A 2×2 $mm^2$ in-plane resolution (Fig. 5a) was obtained for hyperpolarized HEP using indirect proton detection. Total experimental time for proton imaging was on the order of 3 s, consisting largely of the multiband proton presaturation period of 2 s. The $^{1}H$ hyperpolarized image had an SNR of 256 corresponding to 1.41% (corresponding to $\varepsilon_{exp}$ = 900) hyperpolarization of total polarized $^{1}H$ intensity per 0.0098 mM effective concentration, similar to previous studies (13). As with the $^{13}C$ direct detection experiments using $^{13}C$ hyperpolarized HEP, the lifetime of the hyperpolarization was short and hyperpolarization decayed after 90 s to undetectable levels in proton indirect imaging (Fig. 5b).

Examining the theoretical polarization transfer efficiency $\eta$ in HEP from $^{13}C$ to $^{1}H$ was not pursued because in addition to the methyl protons of interest, HEP contains a methylene proton as well. However, we note that 1.41% $^{1}H$ polarization was achieved after polarization transfer from 5.3% polarized $^{13}C$ in HEP corresponding to 27% polarization transfer efficiency $\eta$ calculated as $P_{1H}/P_{13C}$.

## 4. Discussion

### 4.1. Polarization transfer efficiency

When comparing polarization transfer efficiency from $^{1}H$ to $^{13}C$ in 1-$^{13}C$-acetate, $\eta$ differed in the spectroscopic and imaging detection approaches. The difference between 70% and 87% respectively was likely a manifestation of large error in $\eta$ of imaging, because of the relatively low SNR of the reference thermal $^{13}C$ image, Fig. 1c. Therefore, the $\eta$ value derived from the $H \rightarrow {}^{13}C$ spectroscopic study was used in further calculations of $^{13}C \rightarrow H$ polarization $\varepsilon_{exp}$ and $\eta$.

$^{13}C \rightarrow H$ polarization transfer efficiency $\eta$ was lower in the imaging studies of 1-$^{13}C$-acetate/$D_2O$ phantom compared to corresponding spectroscopic studies, 85.7% vs. 98.6%. Moreover, $\eta$ decreased further, down to 45.1% in the case of the 1-$^{13}C$-acetate/$H_2O$ phantom. A likely explanation for such significant decreases in the imaging studies and especially for the case of 1-$^{13}C$-acetate/$H_2O$ is the $T_2$ effect, because RF pulses are applied every 6 ms and non-equilibrium $^{1}H$ polarization transferred from $^{13}C$ is mixed with thermal polarization of protons with relatively short $T_2$. A potential improvement can be achieved through imaging acceleration using faster acquisition. However, frequency selective RF pulses as implemented here represented the largest fraction of total acquisition time. Therefore, more optimal design and implementation of RF excitation pulses with spectral selectivity would potentially improve the overall SNR of indirect proton imaging detection. The latter can be achieved through a variety of solutions. (i) Higher field MRI systems such as ≥9.4 T increase chemical shift dispersion leading to shorter RF pulses with identical frequency selectivity. (ii) Sinc RF pulses or other waveforms can also potentially lead to

NIH-PA Author Manuscript

NIH-PA Author Manuscript

NIH-PA Author Manuscript

shorter RF excitation pulses with similar or better frequency selectivity. (iii) Low field MRI indirect detection potentially allows for significantly lower water background and could potentially eliminate the need for frequency selective RF pulses. For example, it has been shown that high detection sensitivity can be achieved at 0.0475 T, a field that has 100 times less polarized water (25). In that case, simple proton presaturation would perform better and may be sufficient. Regardless of the approach to improve the apparent $\eta$ of $^{13}C \rightarrow H$ for indirect proton imaging, it will significantly increase the detection sensitivity presented here by several fold.

A similar trend in $\eta$ for $^{13}C \rightarrow H$ polarization transfer in hyperpolarized HEP was observed in corresponding imaging experiments, Table. 1. $\eta$ of the imaging study was only 27% and clearly has room for potential improvement.

### 4.2. Spatial resolution improvement

Despite reduced apparent $\eta$ values in the $^{13}C \rightarrow H$ imaging study with 1-$^{13}$C-acetate in water, proton imaging SNR was 145 for a 2×2 mm$^2$ in-plane resolution. This correlates with a SNR of 29.8 and 3×3 mm$^2$ in-plane resolution where $^{13}$C was imaged with the same level of $^{13}$C polarization. We note that the RF coil was not particularly optimized for $^1$H detection. Nevertheless, indirect proton detection yielded 11.0 times the SNR per unit of volume. This proves the underlying hypothesis that indirect proton detection of hyperpolarized compounds is a more sensitive means of imaging. To a certain extent, this rather high value of sensitivity enhancement is enabled by three protons rather than one $^{13}$C carbon, even under conditions of relatively low *Eff*, and $\varepsilon_{exp} \ll 1$. It should also be pointed out that the overall experimentally observed sensitivity enhancement factor of 11.0 described above also reflects $^1$H sensitivity loss due to the implemented RF excitation pulses. Approximately 60% signal loss was observed in the implementation of frequency selective pulses during $^1$H imaging compared to square RF pulses with $\tau_{90^\circ}$ = 57 μs. This shortcoming should be addressed in future studies. However, if properly addressed, SNR gains in excess of 20 fold are potentially achievable.

### 4.3. Limitations and future perspectives, and subject RF noise

The $^{13}C \rightarrow H$ imaging study with $^{13}$C hyperpolarized HEP in water also yielded relatively low $\eta$ of 27%. This compares to $\eta$ = 45.1% in the $^{13}C \rightarrow H$ imaging study with 1-$^{13}$C-acetate in water. The comparison of imaging SNR of direct $^{13}$C and indirect $^1$H studies, Table 1, shows that indirect detection yielded 3.25 times more SNR. The significant discrepancy with the factor of 11.0 described above can be explained by lower $\eta$ value and three acetate protons per molecule compared to the one proton per chemical group in perdeuterated PASADENA addition product of HEA (HEP). Moreover, polarization transfer delays could likely be further optimized to improve experimental transfer yields.

It should also be pointed out that proton detection is conducted at significantly higher frequency, which is one of the contributing factors in the $(\gamma_{1H}/\gamma_{13C})^2$ expression, not accounting for $T_2$, RF coil sensitivity and subject RF noise. While RF coil sensitivity can be optimized for the detection frequency of interest, $T_2$ (31) and subject RF noise (32) are fundamentally unavoidable, but have frequency dependence. Therefore, it is likely that the

NIH-PA Author Manuscript

NIH-PA Author Manuscript

NIH-PA Author Manuscript

efficiency of improved proton detection can decrease with transition to *in vivo* studies, larger sample and subject sizes and higher resonance frequencies. While the increased body noise at greater proton frequencies is a clear limitation of this method (33), we point out that it can be significantly alleviated in the low-field MRI regime, where RF losses and body noise on the clinical subjects is negligible (34). As a result, low-field MRI of hyperpolarized contrast agents in humans is an attractive approach from sensitivity perspective.

Specific absorption rate (SAR) is undesirable, because it leads to heat deposition from RF pulses. The pulse sequence described here is indeed RF pulse intense. However, the polarization transfer block uses only a few high power RF pulses. The remainder of RF pulses, corresponding to excitation RF pulses of FSSFP, are extremely low power (~50 mW). Moreover, the sequence is played only once in less than 1 second. Therefore, SAR is not expected to be an impediment for pre-clinical translation of the presented work at magnetic fields of 4.7 T and lower. However, the clinical translation and high-field preclinical translation will likely result in increased RF pulse power, which could raise SAR concerns. This will likely be exacerbated by 3D applications, where additional RF pulses are needed for 3D encoding. However, it should be stressed that the sequence is ultra-short and power deposition will be limited to ~ 1 second. In case if SAR will exceed the safe limits, a potential solution is to replace FSSFP imaging block by less RF-pulse power intense gradient echo sequences, where a small tipping angle RF pulse is used, i.e. only a small fraction (2–5%) of a full 90° RF pulse is utilized.

The RF pulse width used in frequency selective FSSFP component was > 4 ms, which is sufficiently long for potential clinical translation of this sequence. Because the polarization transfer delays are long due to relatively small heteronuclear spin-spin coupling of isolated $^{13}C$ sites, the RF pulses of polarization transfer block can also be potentially increased as needed (up to the width of frequency selective RF pulses of > 4 ms) for clinical translation.

While the body noise has a negligible contribution to overall NMR noise in low magnetic field (34), the body noise dominates the overall noise at higher frequencies. Because there is more body noise at high frequencies as compared to *in vitro* phantoms, there will be more noise in proton MR compared to $^{13}C$ MR at the same magnetic field. Therefore, the observed SNR gains for indirect proton detection will be reduced *in vivo* at high magnetic fields and frequencies. However, hyperpolarized MRI sensitivity does not gain from higher fields in general and therefore, translation of this approach will be more beneficial at lower fields, i.e. < 4.7 T.

$^{13}C \rightarrow H$ imaging studies used proton background suppression, taking advantage of multiband pre-saturation RF pulses and frequency selective RF excitation pulses, which resulted in an overall increase of experimental time and more importantly imaging time. For example, imaging time increased from 64 ms (no frequency selective pulse) to 192 ms (with frequency selective pulses). As mentioned above, most of the imaging time was spent on RF excitation pulses. While the latter can be potentially decreased by smarter RF pulse design and implementation, the alternative solution is to increase spatial resolution while decreasing the RF pulse width and maintaining the same background level. For example, the

NIH-PA Author Manuscript

NIH-PA Author Manuscript

NIH-PA Author Manuscript

relatively high SNR of 256 with 2×2 $mm^2$ in-plane resolution can be traded for improved spatial resolution with 1×1 $mm^2$, which is also desirable from a cancer imaging perspective, while maintaining relatively high and certainly acceptable levels of SNR.

We anticipate that this work can be readily translated to in vivo imaging of hyperpolarized contrast agents. Indirect imaging of hyperpolarized 1-$^{13}$C-lactate as a metabolic product of injected hyperpolarized 1-$^{13}$C-pyruvate is particularly attractive using the demonstrated strategy. Because of larger chemical shift separation in the $^{13}$C dimension between 1-$^{13}$C-pyruvate and 1-$^{13}$C-lactate > 10 ppm, 1-$^{13}$C resonance of lactate can be selectively excited (35) for polarization transfer to its three methyl protons, while retaining hyperpolarized magnetization of 1-$^{13}$C-pyruvate. Additionally, lactate similarly to the acetate presented here, has three methyl protons and similarly large SNR gains are expected, as much as an order of magnitude as presented here. This can be translated to significantly improved spatial resolution or improved sensitivity of hyperpolarized MR, which are still lacking and can benefit from the improvements described here.

Extension of this method to 3D hyperpolarized imaging (36) can be potentially realized, but challenges need to be addressed including the required short imaging time due to imposed $T_2$ limitations of protons. These limitations can be addressed by decreasing the acquisition time necessary to scan each line of k-space as well as implementing compressed sensing.

A single proton image was recorded for $^{13}$C hyperpolarized contrast agent here, while multiple acquisitions may be desired for kinetics studies of metabolism *in vivo*. The latter can be realized by the use of partial polarization transfer from $^{13}$C to $^{1}$H (23), where only a fraction of long-lived $^{13}$C hyperpolarized is consumed for a single 2D or potentially 3D image, and multiple polarization transfer can enable acquisition of multiple proton images of $^{13}$C hyperpolarized contrast media.

## 5. Conclusion

We have used frequency selective FSSFP method for indirect proton imaging of the aqueous $^{13}$C hyperpolarized contrast agent HEP. Indirect proton imaging allowed for notable sensitivity improvement. Frequency selective RF pulses combined with proton multiband pre-saturation significantly decreased water and other proton background signals to an acceptable level for quantitative imaging, demonstrating that $^{13}$C hyperpolarized MR can significantly benefit from indirect proton sub-second imaging.

SNR gains of up to 11 fold from proton imaging versus direct $^{13}$C imaging were demonstrated with a sodium 1-$^{13}$C-acetate phantom in water, where three methyl protons were used for detection. SNR gain of 3.25 for hyperpolarized HEP was somewhat lower. The demonstrated method can be applied to a number of other hyperpolarized contrast agents including hyperpolarized 1-$^{13}$C-pyruvate and 1-$^{13}$C-lactate, 5-$^{13}$C-glutamine, succinate and others. The demonstrated SNR gains can be further improved significantly by (i) implementation of more suitable frequency selective RF pulses and better chemical shift dispersion at high field or (ii) use of low field MR imaging. We speculate that SNR can be improved by a factor of 2 to 5.

NIH-PA Author Manuscript

NIH-PA Author Manuscript

NIH-PA Author Manuscript

The demonstrated method can potentially be extended to 3D and in vivo application. Moreover, this method of indirect proton detection of hyperpolarized contrast agents solves an important challenge of $^{13}C$ hyperpolarized MR by eliminating the need for $^{13}C$ detection. Conventional proton detection is universally available on clinical MRI scanners and can be utilized for detection of hyperpolarized contrast agents while requiring only $^{13}C$ RF excitation during the polarization transfer sequence. Furthermore, $^{1}H$ imaging is significantly less demanding from the perspective of gradient power requirements.

## Supplementary Material

Refer to Web version on PubMed Central for supplementary material.

## Acknowledgments

**Funding Sources**

We gratefully acknowledge the financial support from NIH/NCI 5R00 CA134749-03, ICMIC 5P50 CA128323-03, R25 CA136440, 3R00CA134749-02S1, NIH EB001628-10, Prevent Cancer Foundation, and Department of Defense CDMRP Era of Hope Breast Cancer Award W81XWH-12-1-0159/BC112431.

## ABBREVIATIONS

| | |
|---|---|
| **PHIP** | parahydrogen induced polarization |
| **HEP** | 2-hydroxyethyl 1-$^{13}C$-propionate-$d_{2,3,3}$ |
| **HEA** | 2-hydroxyethyl 1-$^{13}C$-acrylate-$d_{2,3,3}$ |
| **INEPT** | insensitive nulcei enhanced by polarization transfer |
| **RINEPT** | refocused insensitive nuclei enhanced by polarization transfer |
| **DEPT** | distortionless enhancement by polarization transfer |
| **APT** | attached proton test |
| **FSSFP** | fast stead-state free precession |
| **FOV** | field of view |
| $\eta$ | efficiency |
| **PASADENA** | Para-Hydrogen and Synthesis Allow Dramatically Enhanced Nuclear Alignment |
| **DNP** | dynamic nuclear polarization |

## References

1. Abragam A, Goldman M. Principles of Dynamic Nuclear Polarization. Rep Prog Phys. 1978; 41(3): 395–467.
2. Day SE, Kettunen MI, Gallagher FA, Hu DE, Lerche M, Wolber J, Golman K, Ardenkjaer-Larsen JH, Brindle KM. Detecting tumor response to treatment using hyperpolarized C-13 magnetic resonance imaging and spectroscopy. Nat Med. 2007; 13(11):1382–1387. [PubMed: 17965722]

NIH-PA Author Manuscript NIH-PA Author Manuscript NIH-PA Author Manuscript


3. Ardenkjaer-Larsen JH, Fridlund B, Gram A, Hansson G, Hansson L, Lerche MH, Servin R, Thaning M, Golman K. Increase in signal-to-noise ratio of > 10,000 times in liquid-state NMR. Proc Natl Acad Sci U S A. 2003; 100(18):10158–10163. [PubMed: 12930897]
4. Eisenschmid TC, Kirss RU, Deutsch PP, Hommeltoft SI, Eisenberg R, Bargon J, Lawler RG, Balch AL. Para Hydrogen Induced Polarization In Hydrogenation Reactions. J Am Chem Soc. 1987; 109(26):8089–8091.
5. Cai C, Coffey AM, Shchepin RV, Chekmenev EY, Waddell KW. Efficient transformation of parahydrogen spin order into heteronuclear magnetization. J Phys Chem B. 2013; 117(5):1219–1224. [PubMed: 23214962]
6. Kurhanewicz J, Vigneron DB, Brindle K, Chekmenev EY, Comment A, Cunningham CH, DeBerardinis RJ, Green GG, Leach MO, Rajan SS, Rizi RR, Ross BD, Warren WS, Malloy CR. Analysis of Cancer Metabolism by Imaging Hyperpolarized Nuclei: Prospects for Translation to Clinical Research Neoplasia. 2011; 13(2):81–97.
7. Golman K, in't Zandt R, Thaning M. Real-time metabolic imaging. Proc Natl Acad Sci U S A. 2006; 103(30):11270–11275. [PubMed: 16837573]
8. Chekmenev EY, Hovener J, Norton VA, Harris K, Batchelder LS, Bhattacharya P, Ross BD, Weitekamp DP. PASADENA hyperpolarization of succinic acid for MRI and NMR spectroscopy. J Am Chem Soc. 2008; 130(13):4212–4213. [PubMed: 18335934]
9. Gallagher FA, Kettunen MI, Day SE, Lerche M, Brindle KM. C-13 MR spectroscopy measurements of glutaminase activity in human hepatocellular carcinoma cells using hyperpolarized C-13-labeled glutamine. Magn Reson Med. 2008; 60(2):253–257. [PubMed: 18666104]
10. Bowers CR, Weitekamp DP. Para-Hydrogen and Synthesis Allow Dramatically Enhanced Nuclear Alignment. J Am Chem Soc. 1987; 109(18):5541–5542.
11. Morris GA, Freeman R. Enhancement of Nuclear Magnetic-Resonance Signals by Polarization Transfer. J Am Chem Soc. 1979; 101(3):760–762.
12. Klomp DWJ, Wijnen JP, Scheenen TWJ, Heerschap A. Efficient H-1 to P-31 Polarization Transfer on a Clinical 3T MR System. Magn Reson Med. 2008; 60(6):1298–1305. [PubMed: 19030163]
13. Chekmenev EY, Norton VA, Weitekamp DP, Bhattacharya P. Hyperpolarized (1)H NMR Employing Low gamma Nucleus for Spin Polarization Storage. J Am Chem Soc. 2009; 131(9): 3164–3165. [PubMed: 19256566]
14. Sarkar R, Comment A, Vasos PR, Jannin S, Gruetter R, Bodenhausen G, Hall H, Kirik D, Denisov VP. Proton NMR of N-15-Choline Metabolites Enhanced by Dynamic Nuclear Polarization. J Am Chem Soc. 2009; 131(44):16014. [PubMed: 19848401]
15. Kadlecek S, Vahdat V, Nakayama T, Ng D, Emami K, Rizi R. A simple and low-cost device for generating hyperpolarized contrast agents using parahydrogen. NMR Biomed. 2011; 24(8):933–942. [PubMed: 21845739]
16. Frydman L, Blazina D. Ultrafast two-dimensional nuclear magnetic resonance spectroscopy of hyperpolarized solutions. Nat Phys. 2007; 3(6):415–419.
17. Mishkovsky M, Cheng T, Comment A, Gruetter R. Localized in vivo hyperpolarization transfer sequences. Magn Reson Med. 2012; 68(2):349–352. [PubMed: 22190079]
18. Zeng H, Bowen S, Hilty C. Sequentially acquired two-dimensional NMR spectra from hyperpolarized sample. J Magn Reson. 2009; 199(2):159–165. [PubMed: 19447055]
19. Bastiaansen JAM, Cheng T, Mishkovsky M, Duarte JMN, Comment A, Gruetter R. In vivo enzymatic activity of acetylCoA synthetase in skeletal muscle revealed by C-13 turnover from hyperpolarized 1-C-13 acetate to 1-C-13 acetylcarnitine. Biochim Biophys Acta-Gen Subj. 2013; 1830(8):4171–4178.
20. Jensen PR, Peitersen T, Karlsson M, in't Zandt R, Gisselsson A, Hansson G, Meier S, Lerche MH. Tissue-specific Short Chain Fatty Acid Metabolism and Slow Metabolic Recovery after Ischemia from Hyperpolarized NMR in Vivo. J Biol Chem. 2009; 284(52):36077–36082. [PubMed: 19861411]
21. Mishkovsky M, Comment A, Gruetter R. In vivo detection of brain Krebs cycle intermediate by hyperpolarized magnetic resonance. J Cereb Blood Flow Metab. 2012; 32(12):2108–2113. [PubMed: 22990416]

NIH-PA Author Manuscript

NIH-PA Author Manuscript

NIH-PA Author Manuscript


22. Pfeilsticker JA, Ollerenshaw JE, Norton VA, Weitekamp DP. A selective N-15-to-H-1 polarization transfer sequence for more sensitive detection of N-15-choline. J Magn Reson. 2010; 205(1):125–129. [PubMed: 20472478]
23. Norton VA, Weitekamp DP. Communication: Partial polarization transfer for single-scan spectroscopy and imaging. J Chem Phys. 2011; 135(14)
24. Waddell KW, Coffey AM, Chekmenev EY. In situ Detection of PHIP at 48 mT: Demonstration using a Centrally Controlled Polarizer. J Am Chem Soc. 2011; 133(1):97–101. [PubMed: 21141960]
25. Coffey AM, Shchepin RV, Wilkens K, Waddell KW, Chekmenev EY. A Large Volume Double Channel 1H-X RF Probe for Hyperpolarized Magnetic Resonance at 0. 0475 Tesla. J Magn Reson. 2012; 220:94–101. [PubMed: 22706029]
26. Feng B, Coffey AM, Colon RD, Chekmenev EY, Waddell KW. A pulsed injection parahydrogen generator and techniques for quantifying enrichment. J Magn Reson. 2012; 214(0):258–262. [PubMed: 22188975]
27. Goldman M, Johannesson H. Conversion of a proton pair para order into C-13 polarization by rf irradiation, for use in MRI. C R Physique. 2005; 6(4–5):575–581.
28. Gridnev ID, Higashi N, Asakura K, Imamoto T. Mechanism of asymmetric hydrogenation catalyzed by a rhodium complex of (S,S)-1,2-bis(tert-butylmethylphosphino)ethane. Dihydride mechanism of asymmetric hydrogenation. J Am Chem Soc. 2000; 122(30):7183–7194.
29. Gridnev ID, Imamoto T. On the mechanism of stereoselection in Rh-catalyzed asymmetric hydrogenation: A general approach for predicting the sense of enantioselectivity. Acc Chem Res. 2004; 37(9):633–644. [PubMed: 15379579]
30. Hövener J-B, Chekmenev E, Harris K, Perman W, Tran T, Ross B, Bhattacharya P. Quality assurance of PASADENA hyperpolarization for 13C biomolecules. Magn Reson Mat Phys Biol Med. 2009; 22:123–134.
31. Scheffler K, Hennig J. Is TrueFISP a gradient-echo or a spin-echo sequence? Magn Reson Med. 2003; 49(2):395–397. [PubMed: 12541263]
32. Darrasse L, Ginefri JC. Perspectives with cryogenic RF probes in biomedical MRI. Biochimie. 2003; 85(9):915–937. [PubMed: 14652180]
33. Golman K, Petersson JS. Metabolic imaging and other applications of hyperpolarized C-13. Acad Radiol. 2006; 13(8):932–942. [PubMed: 16843845]
34. Hayden ME, Bidinosti CP, Chapple EM. Specific absorption rates and signal-to-noise ratio limitations for MRI in very-low magnetic fields. Concept Magnetic Res A. 2012; 40A(6):281–294.
35. von Morze C, Sukumar S, Reed GD, Larson PEZ, Bok RA, Kurhanewicz J, Vigneron DB. Frequency-specific SSFP for hyperpolarized C-13 metabolic imaging at 14. 1 T. Magn Reson Imaging. 2013; 31(2):163–170. [PubMed: 22898680]
36. Larson PEZ, Hu S, Lustig M, Kerr AB, Nelson SJ, Kurhanewicz J, Pauly JM, Vigneron DB. Fast Dynamic 3D MR Spectroscopic Imaging With Compressed Sensing and Multiband Excitation Pulses for Hyperpolarized C-13 Studies. Magn Reson Med. 2011; 65(3):610–619. [PubMed: 20939089]

NIH-PA Author Manuscript

NIH-PA Author Manuscript

NIH-PA Author Manuscript

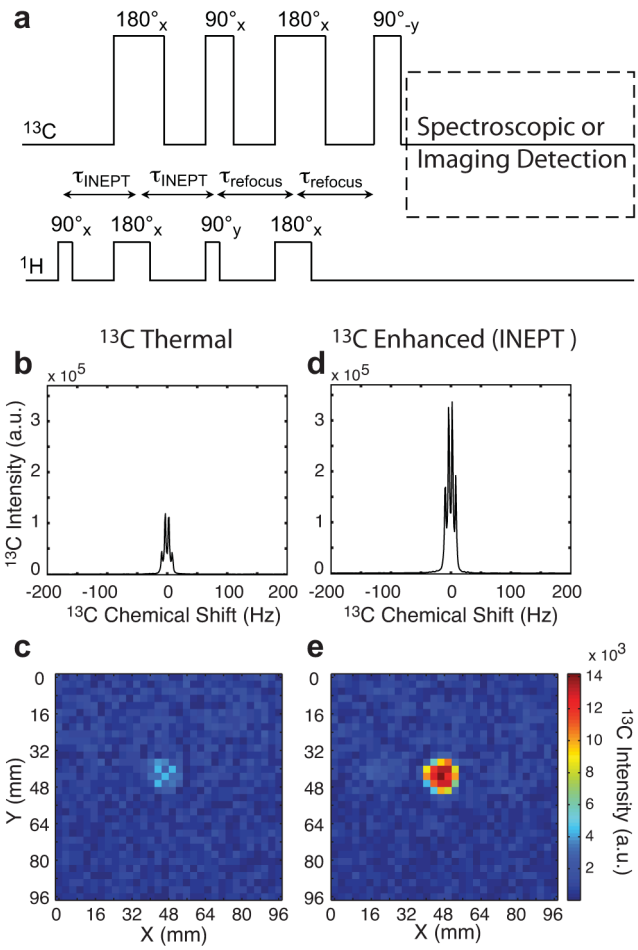


**Figure 1. $^{13}$C Spectroscopy and Imaging of sodium 1-$^{13}$C-acetate**

**(a)** Refocused INEPT sequence. **(b)** $^{13}$C reference spectrum of a thermally polarized 2.8 mL phantom of 4.3 M sodium 1-$^{13}$C-acetate in water using a single scan acquisition, and **(c)** FSSFP projection image. **(d)** $^{13}$C INEPT spectroscopy and **(e)** INEPT enhanced imaging of sodium 1-$^{13}$C-acetate using the sequence shown in **(a)**. All the images were acquired with TR = 2 ms, TE = 1 ms, a field of view (FOV) of 96×96 mm$^2$, and an in-plane resolution of 3×3mm$^2$, with the same contour scaling levels. The following INEPT delays were used $\tau_{INEPT}$ = 42 ms and $\tau_{refocus}$ = 16 ms for polarization from $^1$H→$^{13}$C.

NIH-PA Author Manuscript

NIH-PA Author Manuscript

NIH-PA Author Manuscript

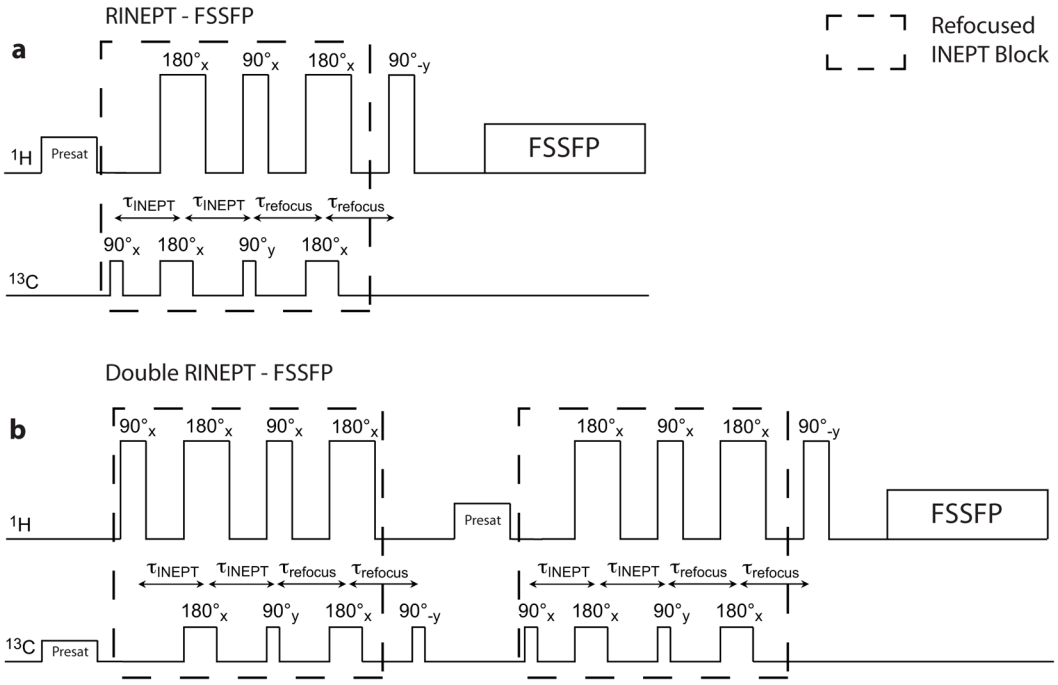


**Figure 2. INEPT Enhanced $^{1}$H FSSFP sequence diagrams**

**(a)** The RINEPT-FSSFP RF pulse sequence contains a 2 s presaturation pulse (Presat), a refocused INEPT block (RINEPT), and FSSFP imaging block using a low power frequency selective Gaussian pulse for detection. $\tau_{INEPT}$ represents the INEPT delay, while $\tau_{refocus}$ is the refocusing delay, **(b)** Double RINEPT-FSSFP RF pulse sequence with extra RINEPT block for prepolarization of $^{13}$C from more polarized protons of thermally polarized phantoms in sodium 1-$^{13}$C-acetate.

NIH-PA Author Manuscript
NIH-PA Author Manuscript
NIH-PA Author Manuscript



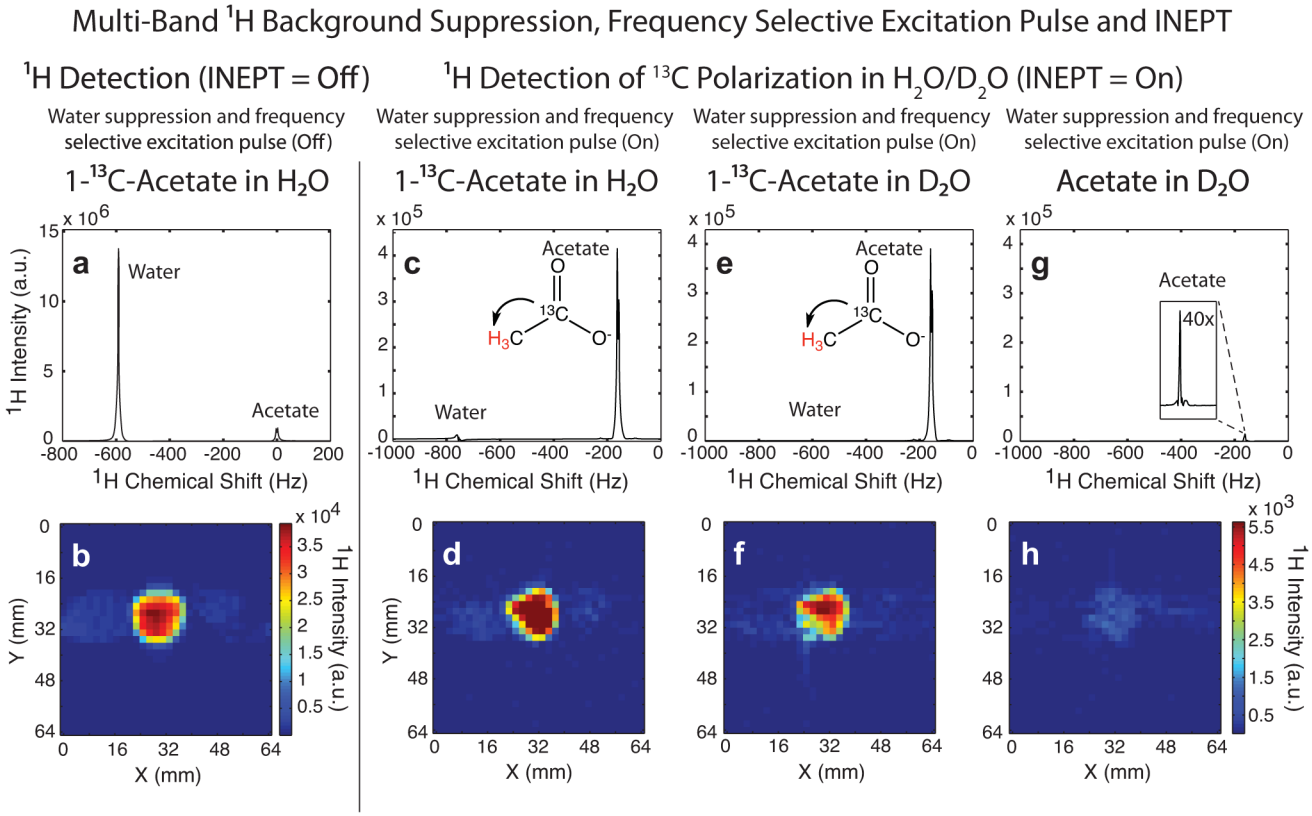


**Figure 3. Indirect $^{1}$H Spectroscopic and Imaging Detection Using INEPT Enhancement**

Single scan $^{1}$H detection of a 2.8 mL phantom of 4.3 M sodium 1-$^{13}$C-acetate in water (**a** and **b**) without background multiband $^{1}$H suppression (Off) or INEPT enhancement (Off). Indirect $^{1}$H detection enhanced by INEPT for spectroscopy, and INEPT enhanced FSSFP for imaging for 2.8 mL phantoms of 4.3 M $^{13}$C-sodium acetate in water (**c** and **d**) and in $D_2O$ (**e** and **f**), and also 4.3 M natural abundance sodium acetate in $D_2O$ (**g** and **h**). A small amount of thermal naturally abundant acetate signal is detected even with background $^{1}$H suppression and can be observed in the inset of (**g**) and faintly in the image (**h**). All the images were acquired using TR = 6.20 ms, TE = 3.10 ms, FOV = 64×64 mm$^2$, and an in-plane resolution of 2×2 mm$^2$.

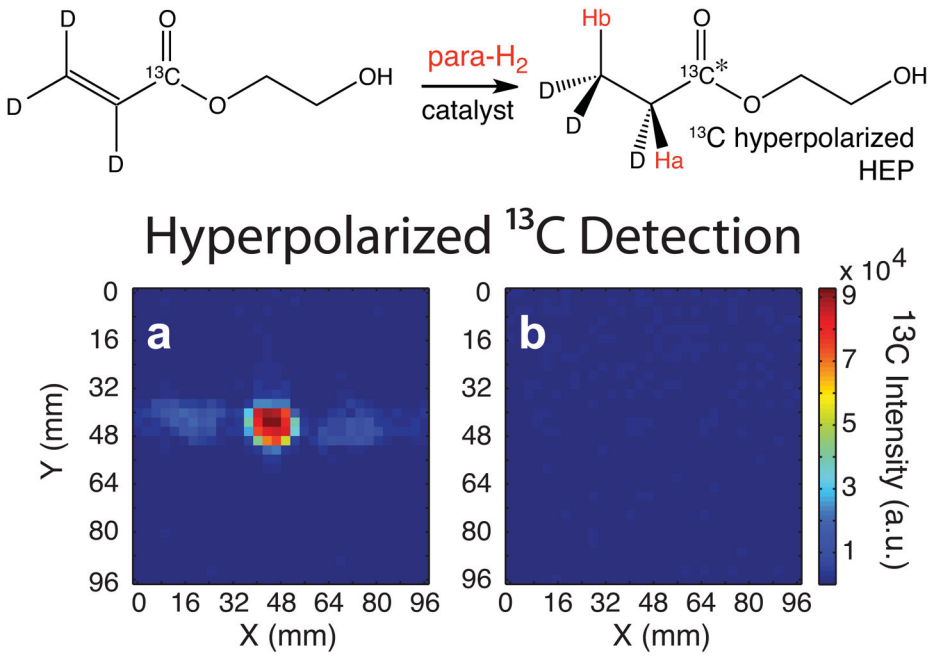


**Figure 4. Hyperpolarized $^{13}$C FSFFP Imaging**

**(a)** $^{13}$C detection of $^{13}$C hyperpolarized HEP using sub-second FSSFP, **(b)** FSFFP image of the "cold" contrast agent 90 s after acquisition shown in (a). Hyperpolarized $^{13}$C images were acquired with TR = 2 ms, TE = 1 ms, a field of view (FOV) of 96×96 mm$^2$, and an in-plane resolution of 3×3 mm$^2$. No extrapolation or zero filling was applied to images or spectra, and images are shown in their raw resolution.



NIH-PA Author Manuscript
NIH-PA Author Manuscript
NIH-PA Author Manuscript

NIH-PA Author Manuscript

NIH-PA Author Manuscript

NIH-PA Author Manuscript

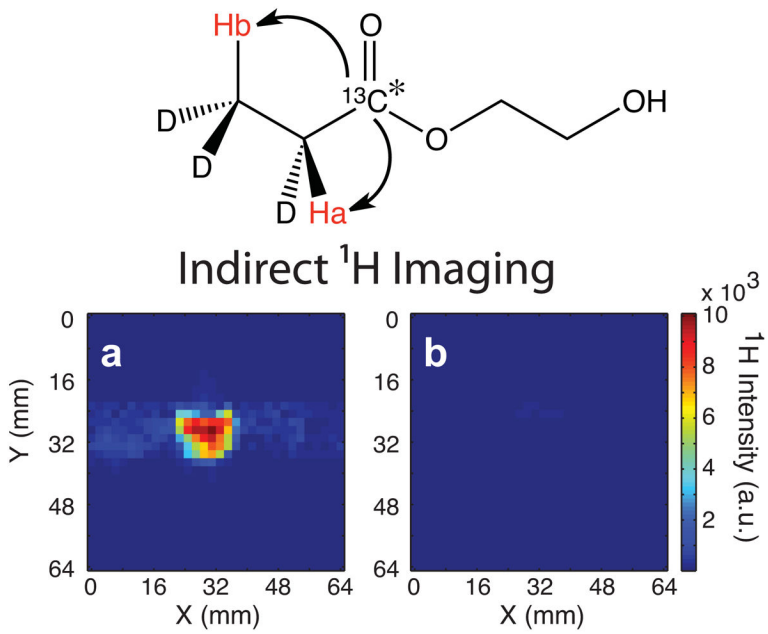


**Figure 5. $^{1}$H Imaging of $^{13}$C Hyperpolarization**

(**a)** Indirect FSSFP $^{1}$H imaging of polarization transferred from $^{13}$C nuclei of $^{13}$C hyperpolarized HEP to neighboring protons using INEPT, **(b)** $^{1}$H image of “cold” state, no detectable signal is observed in the indirect $^{1}$H FSFFP image. Indirect proton images were acquired using TR = 6.35 ms, TE = 3.17 ms, FOV = 64×64 mm$^2$, and an in-plane resolution of 2×2 mm$^2$. No extrapolation or zero filling was applied to images, and images are shown in their raw resolution.

NIH-PA Author Manuscript

NIH-PA Author Manuscript

NIH-PA Author Manuscript

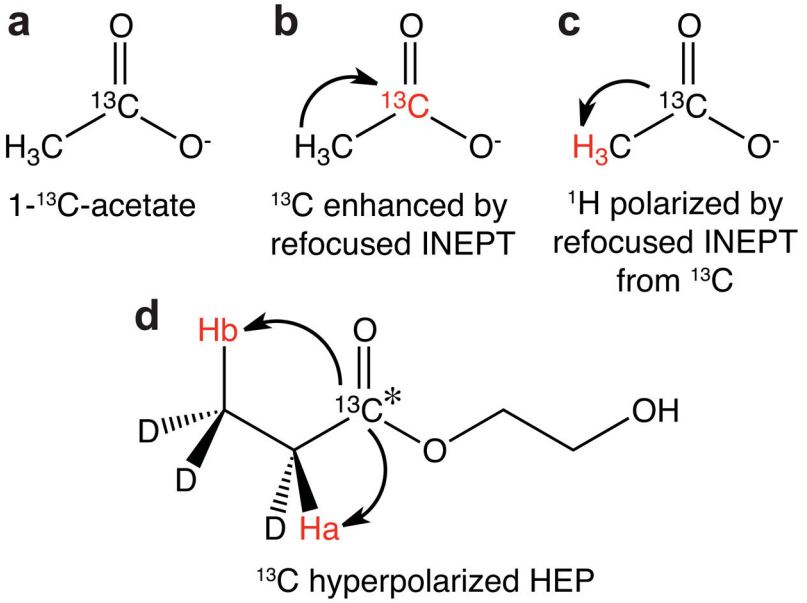


**Figure 6.**
Molecular structures and polarization transfers.

NIH-PA Author Manuscript
NIH-PA Author Manuscript
NIH-PA Author Manuscript



**Table 1**

Summary of the results. Note the error is ±1% unless otherwise noted.

| Transfer | Spatial Resolution | SNR | $^{13}$C Polarization | $^{1}$H Polarization | $\varepsilon_{exp}$ | $\varepsilon_{theory}$ | $\eta$ | $J$ (Hz) |
|---|---|---|---|---|---|---|---|---|
| Sodium 1-$^{13}$C-acetate/$D_2O$ | | | | | | | | |
| $^{13}$C→**H** | Spectroscopy | 6209 | $1.30*10^{-5}$ | $\mathbf{4.75*10^{-6}}$ | 0.367 | 0.372 | 98.6% | 6.0 |
| H→**$^{13}$C** | Spectroscopy | 960 | $\mathbf{1.30*10^{-5}}$ | $1.61*10^{-5}$ | 3.23 | 4.59 | 70.3% | 6.0 |
| $^{13}$C→**H** | 2×2 mm$^2$ | 197 | $1.30*10^{-5}$ | $\mathbf{4.14*10^{-6}}$ | 0.319 | 0.372 | 85.7% | 6.0 |
| H→**$^{13}$C** | 3×3 mm$^2$ | 29.8 | $\mathbf{(1.61±0.3)*10^{-6}}$ | $1.61*10^{-5}$ | 3.99±0.6 | 4.59 | 87±15% | 6.0 |
| Sodium 1-$^{13}$C-acetate/$H_2O$ | | | | | | | | |
| $^{13}$C→**H** | 2×2 mm$^2$ | 145 | $1.30*10^{-5}$ | $\mathbf{2.17*10^{-5}}$ | 0.167 | 0.372 | 45.1% | 6.0 |
| $^{13}$C hyperpolarized HEP | | | | | | | | |
| $^{13}$C→**Hb** | 2×2 mm$^2$ | 256 | $(5.3±0.5)*10^{-2}$ | $\mathbf{(1.41*±0.14)*10^{-2}}$ | 900±90 | - | - | 5.6, 7.3 |
| **$^{13}$C** | 3×3 mm$^2$ | 177 | $\mathbf{(5.3±0.5)*10^{-2}}$ | - | 13,200±1,300 | - | - | - |